UNIVERSITÀ DI PISA

Singular Spectrum Analysis and Adaptive Filtering: A Novel Approach for Assessing the Functional Connectivity in fMRI Resting State Experiments

Ph.D. thesis (SSD: ING-INF/06)

Ph.D. course in Automation, Robotics and Bioengineering

Ph.D. Cycle: XXIV (2009-2011)

Tutor:

Prof. Alberto Landi

Ph.D. Student:

Dr. Paolo Piaggi

Department of Energy and Systems Engineering (DESE)

University of Pisa, Pisa, Italy

Abstract

Functional Magnetic Resonance Imaging (fMRI) is used to investigate brain functional connectivity at rest after filtering out non-neuronal components related to cardiac and respiratory processes and to the instrumental noise of MRI scanner. These components are generally removed at their fundamental frequencies through band-pass filtering of the Blood-Oxygen-Level-Dependent (BOLD) signal (low-frequency band – LFB: 0.01–0.10 Hz) while General Linear Model (GLM) is usually employed to suppress slow variations of physiological noise in the LFB, using a signal template derived from non-neuronal regions (e.g. brain ventricles). However, these sources of noise exhibit a non-stationary nature due to the intrinsic time variability of physiological activities or to the nonlinear characteristics of MRI scanner drifts: at present, the standard procedure (band-pass filtering and GLM) does not take into account these noise properties in the processing of BOLD signal.

This thesis proposes the joint usage of two methods (Singular Spectrum Analysis – SSA – and adaptive filtering) that takes advantage of their statistical and time flexibility features, respectively. Indeed SSA is a nonparametric technique capable of extracting amplitude and phase modulated components against a null hypothesis of autocorrelated noise, while the adaptive filter removes the noise correlated to a reference signal, exploiting its non-stationary properties.

The novel procedure (SSA and adaptive filtering) was applied to eight resting state recordings and compared to the standard procedure. The functional connectivity between homologous contralateral regions was then estimated in the LFB using a multivariate correlation index (the RV coefficient) and assessed on preselected grey (GM) and white matter (WM) regions of interest (ROIs). A corrected version of the RV coefficient for the number of voxels was developed and used to compare the functional connectivity estimates obtained by the standard procedure (using all available voxels) and from the novel procedure based on the voxel time courses with significant SSA components in the LFB (active voxels).

The adaptive filtering showed a greater reduction of noise compared to GLM (average signal variance decrease in all ROIs: −43.9% vs. −10.1%), using a non-stationary noise template obtained from brain ventricles signals in the LFB. The functional connectivity quantified by the RV coefficient and estimated on the active voxels identified by SSA showed a higher contrast between GM and WM regions with respect to the standard procedure (35% vs. 28%).

These results suggest that SSA and adaptive filtering may be a feasible procedure for properly removing the physiological noise in the LFB of BOLD signal and for highlighting resting state functional networks.

Keywords: Adaptive filtering, Autocorrelated Noise, BOLD signal, Functional Connectivity, Nonstationarity Test, Principal Component Analysis, Resting State, RV Coefficient, Singular Spectrum Analysis.

TABLE OF CONTENTS

1. INTRODUCTION

Functional Magnetic Resonance Imaging (fMRI) is commonly used to describe the dynamics of brain activity during task-activation experiments [1, 2], resting wakefulness [3-5] and sleep [6]. Resting state fMRI studies have demonstrated that the neuronal activity is indirectly reflected in amplitude changes of the Blood Oxygen Level-Dependent (BOLD) signal, which are prominent in the low-frequency band (LFB, f <0.1 Hz) [3, 7] and show temporal synchronizations between spatially remote brain areas, including homologous areas (the so-called *functional connectivity* [8]). The study of the coherence of these slow spontaneous fluctuations of BOLD signal led to the identification of several resting state networks such as the motor [3], the visual [9], the auditory and the attentional networks [10-12], as well as the *default mode* network [13] which comprise brain regions showing high correlation at rest and decreased activity during operative tasks [14-16].

Two main strategies are usually employed to obtain functional connectivity maps [17]: the *seed voxel* approach [3-5] and the Independent Component Analysis (ICA) modified for fMRI data [18, 19]. The former method consists in choosing a small Region of Interest (ROI) from which a reference signal is extracted (typically by averaging the time courses of the voxels within the ROI) and assessing its temporal correlation with the signals belonging to other ROIs. Differently, ICA is a data driven technique that separates noise from the signal of interest, taking advantage of the statistical independence of the noise sources from the BOLD neuronal correlates. Both approaches have demonstrated their efficacy in several experimental protocols [10, 14, 16, 20, 21], nevertheless they also show some limitations. The seed voxel analysis is highly dependent from the specific seed ROI, while the ICA approach, although it doesn't require *a priori* definition of ROIs, is limited by the number of components to retain in the final solution (e.g. a large number of components yields to the oversplitting of one brain network over many maps) and from introducing *a-priori* criteria to discriminate maps related to neuronal activity from those related to the noise components of BOLD signal.

Actually, BOLD signal contains several sources of noise whose power is often larger than the power of sources related to the neuronal activity: these nuisance components can be grouped in two classes, *random* and *physiological* noise. The former class is mainly related to the MRI scanner instability and to thermal noise, both having a wide-spread power spectrum biased towards low frequencies, while the latter is associated to physiological processes such as respiratory (~0.25 Hz) and cardiac (~1 Hz) rhythms. In order to remove these non-neuronal components from BOLD signal, various processing techniques have been proposed: some authors used a band-pass (0.01 Hz to 0.10 Hz) time filter [12, 14, 16, 22], others employed a parametric detrend with a low-pass filtering [4, 23, 24].

However, since the physiological noise slow variability and/or the slow components of the instrumental noise fall in the same frequency band of the BOLD neuronal correlates, none of the above mentioned methods is able to remove such noise. Indeed, besides the neuronal related ones, other sources of slow (<0.1 Hz) BOLD signal oscillations are associated to the heart rate variability [25, 26], to slow variations of respiratory rate [27] and to changes of arterial carbon dioxide level [28]. The issue of removing these slow noise components is classically approached with the Nuisance Variable Regression (NVR) method [29], which is based on estimating a General Linear Model (GLM) [30] including the nuisance regressors as covariates. In fact, this method removes the noise contribution within each BOLD signal using a reference signal derived from non-neuronal regions within the brain such as ventricles [12], or using a direct recording of the noise source (e.g. ECG, respirogram etc.) [27]. Despite its extensive usage, the NVR technique based on the GLM has a limitation in the fact that it does not take into account the nonstationarity of physiological noise (e.g. heart and respiratory rate variabilities [31]), therefore the noise is not properly removed from the BOLD signal. The impact of this limitation is negligible for traditional activation paradigms but it becomes crucial for the study of functional connectivity, both during tasks and in resting state [20, 32].

In order to overcome the above mentioned limitations, this thesis proposes a new procedure for processing the BOLD signal that comprises the Singular Spectrum Analysis (SSA) [33] and the adaptive filtering [34]. SSA is a data driven technique for decomposing the BOLD signal in uncorrelated components while adaptive filtering is based on a time filter whose coefficients can vary as a function of a reference signal, tailored to remove the non-stationary noise in the LFB. Herein it's shown that SSA allowed the identification of *real* oscillatory components compared to an autocorrelated model of noise, namely the SSA components whose signal power was significantly greater than that of the expected components in the null hypothesis of pure noise. It must be underlined that only a fraction of voxels contained genuine oscillations in the LFB that should correspond to the activities of physiological processes, both to the BOLD-related neuronal activity and to the hemodynamic/respiratory slow components of physiological noise: therefore these voxels were considered as *active,* without using any specific task paradigms but assessing the real presence of slow oscillations using a statistical test. The adaptive filtering then served to filter out the non-neuronal components from the time courses of *active* voxels, hence running the functional connectivity analysis on the neuronal components. In order to demonstrate its feasibility, the novel procedure (SSA & adaptive filtering) was compared to the standard approach (band-pass filtering & NVR) by applying both methodologies to the same dataset of real fMRI recordings and by evaluating the functional connectivity between homologous contralateral regions at rest. The temporal synchronization of these regions was quantified using a generalized, multivariate correlation index defined between matrices of signals (instead of the bivariate correlation between pair of voxels), named RV coefficient.

2. METHODS

2.1 Singular Spectrum Analysis

The Singular Spectrum Analysis (SSA) is a data analysis technique that decomposes a time series to obtain a set of distinct uncorrelated components - named Reconstructed Components (RCs) in SSA jargon – which consist in slow-varying trends and in oscillatory components, whose sum is equal to the original time series [33, 35]. SSA was originally proposed to study the meteorological variability, and it has been widely applied both in life sciences as well as in nonlinear physics and signal processing (see [36] and [33] for a complete list of SSA applications). SSA best deals with short and noisy time series where it performs a signal-to-noise ratio enhancement without using *a priori* knowledge of the underlying process (e.g. the resting state condition). In particular, SSA is a nonparametric technique capable of detecting amplitude and phase modulated oscillations and nonlinear trends in the time series.

The algorithm of SSA is based on the decomposition of the *trajectory* (or *embedding*) matrix: given a fixed time window whose length (W) is *a priori* defined, each row of the trajectory matrix is built with overlapping, one-sample-delayed portions of the time series using the sliding window. Thus, the first row of the trajectory matrix contains the first W samples of the time series within the time window, then the window is shifted by one sample and the second row of the matrix is filled in the same way, and so on until the end of the signal is reached. The Principal Component Analysis (PCA) [37] is then applied on the trajectory matrix in order to obtain a set of eigenvalues and associated eigenvectors (*decomposition* step of SSA). These eigenvectors – named Empirical Orthogonal Functions (EOFs) – represent the uncorrelated components of the trajectory matrix, whose signal variance is equal to the corresponding eigenvalue. Finally, from each EOF of the trajectory matrix, the corresponding RC is derived using a least-square algorithm (*reconstruction* step of SSA, see paragraph 2.1.1 for a detailed description of the entire algorithm).

Classically, the signal-to-noise separation is achieved by truncating the *scree* plot of magnitude ordered eigenvalues and by selecting only the elements with the greatest variance [38, 39]: from the EOFs associated to these elements, the significant RCs are then derived and summed for obtaining the extracted signal. However, this procedure is appropriate only in the case of additive white noise (i.e. whose power is independent from frequency) but it fails in the case of an autocorrelated, random noise [40]. Indeed, the BOLD signal is corrupted from several sources of autocorrelated noise such as ultra-low frequency drifts due to MRI scanner instabilities along with movements-related artifacts [29].

The present application assumes a model of autocorrelated (red) noise and uses a modified version of SSA called Monte Carlo SSA [40] (see paragraph 2.1.1 - point F for details about modifications of the original algorithm). This includes an estimation of noise parameters from data (variance and lag-1 autocorrelation) and a statistical test for identifying the significant EOFs, thus it provides a criterion to discriminate the *genuine* oscillatory components from those compatible with a null hypothesis of pure noise. Since the power spectrum of red noise is biased towards low frequencies [41], this operation represents a stringent statistical test for the effective presence of oscillations in the LFB (<0.1 Hz).

The application of SSA to BOLD signals allows identifying *active* voxels at rest as those whose time course contains at least one significant RC in the LFB, thus without using a task paradigm as in the case of task-activation fMRI experiments. In order to identify and retain only the slow-varying components, the dominant frequency of each significant RC was estimated by means of an autoregressive (AR) model, using the Maximum Entropy Method [42]. The dominant frequency was obtained by using a low-order AR model, exploiting the signal-to-noise enhancement provided by SSA [43]. Data analysis software for SSA algorithm was compiled in MATLAB (MathWorks, Natick, MA).

2.1.1 SSA algorithm

The entire SSA algorithm operates in five steps (A-E).

A. Embedding step

A trajectory matrix **D** is derived from the BOLD signal **S(*t*)** of length N, centered on its mean, by using a time window of length W. The i^{th} column of **D** contains the samples of **S(*t*) -** from **S(*i*)** to **S(*i*+W−1)**. The choice of window length – that can be set from 2 to N/2 [43] - is a compromise between the number of signal portions and the frequency resolution. In the lack of a priori hypothesis, a rule of thumb indicates a value ranging from N/5 and N/3 in order to obtain a reliable estimate for oscillatory components [36]. The number of the columns of **D** is equal to M = N−W+1, hence **D** has a Hankel matrix structure of dimension W×M.

From **D**, the lag-covariance matrix $\mathbf{C_V} = \eta \cdot \mathbf{D}\mathbf{D}^T$ of dimension W×W is derived, where ^{T} indicates the matrix transpose operation and the normalization constant η is equal to 1/M.

B. Decomposition step

The lag-covariance matrix $\mathbf{C_V}$ obtained from the initial time series is diagonalized as:

$$\Lambda_V = E_V^T C_V E_V \tag{1}$$

where $\mathbf{\Lambda_V}$ is the data eigenvalue matrix with elements λ_V along the main diagonal in decreasing order of magnitude, while $\mathbf{E_V}$ is the matrix of associated data eigenvectors (EOFs, columns of $\mathbf{E_V}$). The dominant frequency of each EOF is estimated as that with the maximum spectral power in the frequency domain.

C. Statistical test based on the null hypothesis of red noise

The BOLD signal **S(*t*)** is assumed to be composed by oscillations with different frequencies embedded in a red noise background. For the latter, an AR(1) model was considered, which also inherits the case of uncorrelated white noise with a suitable choice of process parameters. The recursive equation that describes the red noise model is:

$$u_t - u_0 = \gamma\left(u_{t-1} - u_0\right) + \alpha z_t \tag{2}$$

where u_0 is the process mean, γ and α are the process parameters (i.e. the lag-1 autocorrelation and variance of red noise, respectively) and z_t is a Gaussian white noise with unit variance. In the case of $\gamma = 0$ (no autocorrelation), the model downgrades to a white noise model. The estimation of the red noise parameters (γ and α) from **S(*t*)** is performed by a maximum likelihood algorithm using unbiased estimators [40].

In a red noise context, the signal-to-noise separation is performed exploiting its autocorrelation properties of the red noise: to this aim, the analytic covariance matrix of red noise $\mathbf{C_N} = c_0\mathbf{T}$ is derived using the estimated noise parameters, where c_0 is the noise variance and elements of $\mathbf{T}_{ij} = \gamma^{|i-j|}$ (i and j are time-lag indexes) [41]. The theoretical EOFs of the red noise are then obtained by diagonalizing $\mathbf{C_N}$ as:

$$\Lambda_N = E_N^T C_N E_N \tag{3}$$

Due to the analytic structure of the noise covariance matrix, the dominant frequencies of $\mathbf{E_N}$ are regularly spaced in the spectrum, separated by ~1/(W×T_c) where T_c is the sampling time. Also, the noise EOFs (columns of $\mathbf{E_N}$) show a sinusoidal behavior in time.

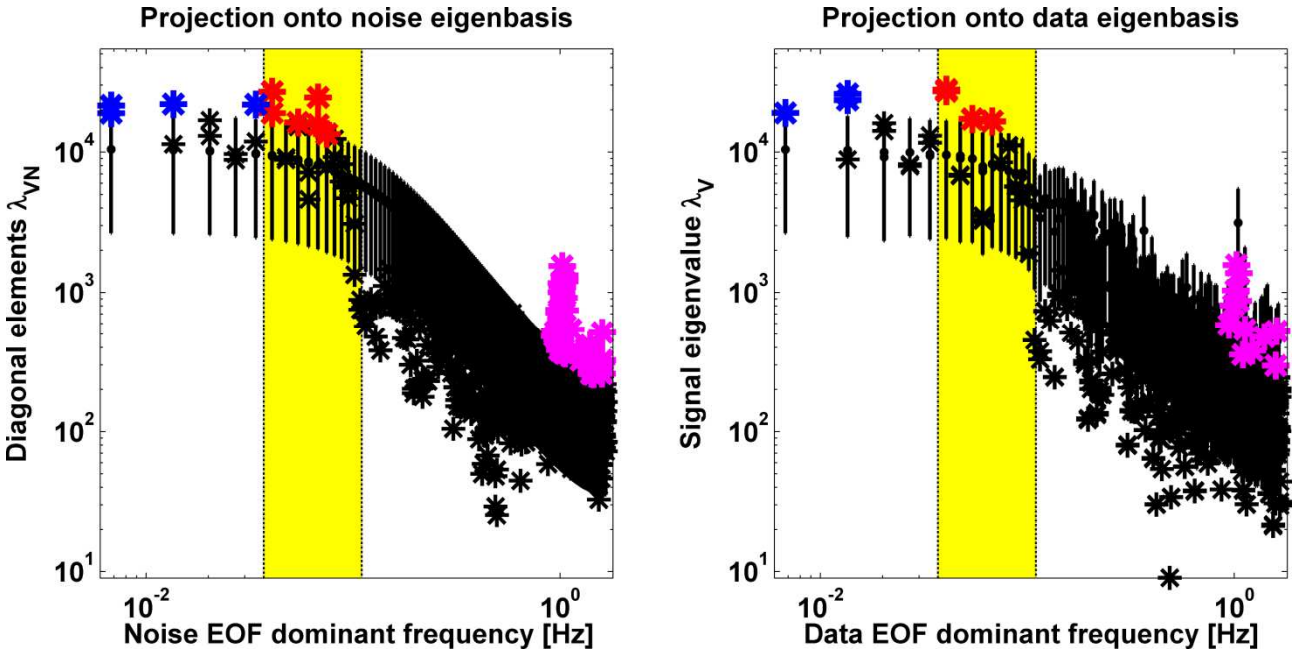

Figure 1. Identification of significant SSA components in the BOLD time course of Figure 2.

<u>Left panel.</u> Eigenspectrum based on noise eigenbasis. The dominant frequency of each theoretical noise EOF (E_N, x-axis) is plotted against the diagonal elements of Λ_{VN} (y-axis, see C1 step). Error bars for noise eigenvalues are derived using the χ^2 distribution and expressed as mean with 95% confidence interval. Significant elements of Λ_{VN} which showed a value greater than the 97.5th percentile of the corresponding noise eigenvalue λ_N (i.e. lying above the error bar) are highlighted and identified as significant trend (blue asterisks), LFB (red asterisks) and cardiac (violet asterisks) components, according to their dominant frequency. The LFB (0.04-0.10 Hz) is highlighted in yellow; nonsignificant elements are drawn as black asterisks.

<u>Right panel.</u> Eigenspectrum based on data eigenbasis. The dominant frequency of each data EOF (E_V, x-axis) is plotted against the data eigenvalues λ_V (y-axis, see C2 step). Error bars for diagonal elements of Λ_{NV} are derived using the χ^2 distribution and expressed as mean with 95% confidence interval. Significant

data eigenvalue λ_V which showed a value greater than the 97.5th percentile of the corresponding diagonal elements of Λ_{NV} (i.e. lying above the error bar) are highlighted and identified as significant trend (blue asterisks), LFB (red asterisks) and cardiac (violet asterisks) components, according to their dominant frequency. The LFB (0.04-0.10 Hz) is highlighted in yellow; nonsignificant elements are drawn as black asterisks.

From each significant EOF of data eigenspectrum (right panel) whose dominant frequency was also found significant in the noise eigenspectrum (left panel), the corresponding RC was calculated. All RCs related to each band (trend, LFB and high frequencies) were summed for obtaining the extracted signals shown in Figure 3 (blue, red and violet lines, respectively).

C1. Projection on noise EOFs

Under the assumptions of Gaussian noise distribution and sinusoidal EOFs, each diagonal element λ_N of $\mathbf{\Lambda_N}$ has a χ^2 distribution with υ = 3N/W degrees of freedom [40]. These assumptions are valid for AR(1) processes and lead to the following distribution for the noise eigenvalues:

$$\lambda_N \approx \left(E_N^T C_N E_N\right)\frac{\chi^2(\nu)}{\nu} \tag{4}$$

From the 2.5th and 97.5th percentiles of these distributions, the 95% confidence interval can be derived for each λ_N. The data covariance matrix $\mathbf{C_V}$ is then projected onto noise EOFs $\mathbf{E_N}$ as:

$$\Lambda_{VN} = E_N^T C_V E_N \tag{5}$$

Assuming a null hypothesis of pure noise that have generated **S(*t*)**, all diagonal elements λ_{VN} of $\mathbf{\Lambda_{VN}}$ should lie within the noise confidence intervals of the related λ_N. Otherwise, the noise EOFs

associated to the λ_{VN} lying outside the corresponding confidence interval, are considered not compatible with the noise model and thus they indicate the presence of real oscillatory components at those frequency (see Figure 1, left panel).

C2. Projection on data EOFs

Since the noise EOFs $\mathbf{E_N}$ are not directly related to the data EOFs $\mathbf{E_V}$, the analytic covariance matrix of red noise $\mathbf{C_N}$ is also projected onto data EOFs as:

$$\Lambda_{NV} = E_V^T C_N E_V \tag{6}$$

Similarly to *C1* step, confidence intervals of the diagonal elements λ_{NV} of $\mathbf{\Lambda_{NV}}$ are derived using (4): accordingly, all data eigenvalues λ_V greater than the corresponding 97.5th percentile of λ_{NV} are considered statistically significant from noise (see Figure 1, right panel).

C3. Assessing the significance of data EOFs

Each data EOF of $\mathbf{E_V}$ that satisfied both these conditions:

1) whose associated noise EOF of $\mathbf{E_N}$ (i.e. with the same dominant frequency) had the corresponding λ_{VN} element greater than the 97.5th percentile of the distribution of the related noise eigenvalue λ_N (step *C1*);
2) whose corresponding data eigenvalue λ_V was greater than the 97.5th percentile of the distribution of the corresponding λ_{NV} element (step *C2*);

were considered globally significant and $\mathbf{E_V^*}$ was the matrix with only the significant data EOFs as columns.

D. Reconstruction step

The projection of original signal **S(*t*)** onto significant data EOFs ($\mathbf{E_V^*}$ matrix) yields the corresponding Principal Components (PCs) matrix $\mathbf{A_V^*}$, as following:

$$A_V^*(t) = \sum_{j=1}^{W} S(t+j-1) \cdot E_V^*(j) \tag{7}$$

For each significant EOF, the corresponding Reconstructed Component (RC) matrix $\mathbf{R_V}^*$ is obtained by:

$$R_k^*(t) = \frac{1}{M_t} \sum_{j=L_t}^{U_t} A_k^*(t-j+1) \cdot E_k^*(j) \tag{8}$$

where M_t, L_t and U_t are time index *t* dependent parameters [43], necessary to manage border effects due to the finite window length W.

E. Dominant frequency estimation

The Maximum Entropy Method (MEM) was used to estimate the dominant frequency of each significant RC. MEM is a spectral analysis method that is based on approximating the time series with a linear autoregressive process of order *M*, i.e., AR(*M*) where *M* is the order of the AR model [42]. The RCs were approximately pure oscillations, thus a low-order all-pole model was used for a consistent estimation of the dominant frequency [43].

F. Modifications of the original Monte Carlo SSA algorithm

In the original procedure proposed by Allen and Smith [40], *C2* step of SSA algorithm using the analytic covariance matrix of red noise $\mathbf{C_N}$ was not clearly employed. Indeed the Monte Carlo approach was used for generating red noise surrogates with the same process parameters, in order to derive the confidence intervals used in the statistical tests and, also, for the correction of type-1

errors due to multiple tests with a great number of EOF (see paragraph 4.2 of Allen and Smith's article). The significant data EOFs were then selected as those with the highest pairwise correlation with their respective noise EOFs (see paragraph 5.2), using the procedure of step *C1*.

Since BOLD signals with a lower TR have greater number of samples and a longer time window is needed in order to extract slow-varying components, the Monte Carlo approach represents a heavy computation burden for the decomposition of all acquired time courses. In addition, a longer time window is associated to a greater number of SSA components, hence requires stringent corrections for type-1errors due to the large number of potentially significant EOFs. On the other hand, the approach of using joint information resulting from noise and data EOF projections, gave the same results of those obtained by the Monte Carlo procedure applied to artificial generated signals in a red noise background (results for artificial signals not shown). Therefore, the present procedure of selecting significant EOFs in the SSA context was proved to be reliable and computationally faster when analyzing BOLD signals for a great number of acquired voxels.

2.2 Adaptive filtering

In the neuroimaging field, the adaptive filtering technique has been successfully applied to near infrared spectroscopy (NIR) for suppressing the global hemodynamic response, hence improving the contrast-to-noise ratio in NIR experiments [44]. Herein, adaptive filtering was employed for removing the non-neuronal components in the LFB of BOLD signal (<0.1 Hz), since their bandwidth overlaps with those related to neuronal activity. These nuisance components are related to the variability of cardiac rate and of respiratory flow [25-28, 45], so they represent the slow variability of physiological noise in the LFB.

Similarly to the NVR approach which employs the GLM technique [29], the adaptive filter removes the noise component on the basis of a reference signal obtained from brain regions where no neuronal activity is expected. To this aim, the time courses of brain ventricles – where pulsatility of cerebrospinal fluid is related to cardiovascular processes [46] – were selected and submitted to PCA. The first principal component (PC) – which accounts for the most part of data variance – was selected as a reference signal for non-neuronal noise and used as the input of the adapting filter.

Adaptive filtering is generally used for system identification, signal prediction and noise cancellation. For the latter, the system block diagram is:

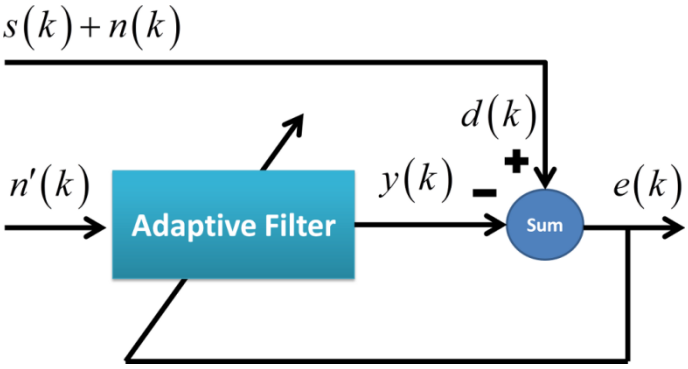

The aim of this procedure is to remove the noise *n(k)* from the information signal *s(k)*. To achieve this goal, a noise reference signal *n'(k)* is fed as input to the adaptive filter in order to suppress its contribution from the desired signal *d(k)*. The desired signal of the adaptive filter is the information signal *s(k)* plus the additive noise *n(k)*, which is a correlated version of *n'(k)*: the adaptive algorithm for filter coefficients relies on reducing the error between the output signal *y(k)* and the desired signal *d(k)* leading to *e(k)*, a cleaned version of *d(k)*, theoretically equal to *s(k)*.

The Least-Mean-Square (LMS) algorithm is the most used linear adaptive filtering procedure for estimating the optimal values of filter weights based on the error signal of the filter. This algorithm consists in two steps:

1) after initializing the values of filter coefficients, the filtering process produces the output signal of the adaptive filter. The error signal *e(k)* is then derived comparing the output signal *y(k)* to the desired signal *d(k)*;

2) the adaptive algorithm is run for the automatic adjustment of filter coefficients, in accordance to the error signal *e(k)* obtained in the previous step.

The adaptive filter used in the present application was a digital Finite Impulse Response (FIR) filter whose coefficients were adjusted over time as a function of time-varying characteristics of the input signal [47]. In order to avoid noise amplification issues, the the *normalized* LMS algorithm [34] was employed for the calculation of filter coefficients. The adaptation formula of the *normalized* LMS (nLMS) algorithm was:

$$w(k+1) = w(k) + \mu \frac{n'(k)}{a + \left\| n'(k) \right\|^2} e^*(k)$$

where *w(k+1)* and *w(k)* were the future and the current vector of filter coefficients, respectively; *n'(k)* and *e(k)* the input and the error signals (respectively), μ was the adaptation step

size and *a* was a small positive constant to overcome potential numerical instability. In the *normalized* version of LMS algorithm – which uses a normalization term $\| n'(k) \|^2$ equal to the squared Euclidean norm of the input signal to avoid noise amplification problems in case *x(k)* is large – the step size can range from 0 to 2 and it was set in order to guarantee the convergence of the solution in all processed signals.

2.3 RV coefficient

The RV coefficient [48] provides a measure of similarity between two signal matrices with the same number of rows (i.e. same number of time points), and putative different number of columns (i.e. number of voxels in this application). It has been used in the fMRI context for testing brain functional connectivity mapping [49], for detecting common activations among subjects [50] and for classifying different experimental conditions within the same subject recording [51].

The RV coefficient is a multivariate generalization of Pearson product-moment correlation, behaving as a cosine between matrices thus taking positive values between 0 (when there is no correlation between each pair of columns in the matrices) and 1 (when there is a perfect correspondence between the two matrices). Being *X* the matrix of BOLD signals in a specific ROI and in a given hemisphere with *n* rows (corresponding to the time points of the acquisition) and *p* columns (corresponding to the number of acquired voxels in the ROI), and being *Y* the matrix related to the homologous contralateral ROI with the same number of rows but different number of columns, the RV coefficient is defined as:

$$RV = \frac{trace\left(XX^{T}YY^{T}\right)}{\sqrt{trace\left(XX^{T}\right)\cdot trace\left(YY^{T}\right)}}$$

where the *trace* operator is defined as the sum of elements on the main diagonal.

In this work, the RV coefficient was employed as a measure of functional connectivity at rest between pairs of matrices of homologous brain regions in different hemispheres. Moreover, it was used for the comparison of the connectivity estimates related to different procedures of BOLD signal processing, applied to the same fMRI dataset. However, the RV coefficient depends on the number of columns in the two matrices, namely it increases with the number of voxels. Actually, in the case of data processed by SSA, the number of voxels within each ROI was smaller since SSA restricted the analysis only to the *active* voxels. In order to overcome this limitation, an algorithm

for correcting the value of RV coefficient (named *corrected* RV coefficient) was developed, resulting from the following resampling procedure.

Given the data processed with the standard approach in a pair of contralateral ROIs with N_L and N_R the total number of voxels of whom N_{aL} and N_{aR} *active* voxels in left and right hemisphere, respectively, 10000 pairs of surrogate signal matrices were generated. The signals in each surrogate matrix were drawn from the complete matrix of all voxels by using a sampling-without-replacement algorithm, so each surrogate matrix contained N_{aL} or N_{aR} signals (according to the related hemisphere). The RV coefficient was then calculated for each pair of matrices in order to obtain the distribution of coefficients related to this surrogate dataset. The 2.5^{th} and the 97.5^{th} percentiles of this distribution were used as references for the comparison with the RV coefficient estimated from data processed by SSA & adaptive filtering. Finally, the *corrected* RV coefficient between homologous contralateral ROIs was taken as the mean value of the distribution.

3. PROCEDURES OF DATA ANALYSIS

In this section, it's shown how the previously described methods were employed in order to process BOLD signals acquired in resting state and to estimate the functional connectivity between preselected ROIs. The analyses have been performed following two parallel flows as shown in Figure 2: the *standard procedure* - including band-pass filtering & NVR - was compared to the *novel procedure* based on SSA & adaptive filtering. Both flows of processing aimed at focusing the connectivity analyses in the LFB after removing the non-neuronal slow components, estimated from the time courses of brain ventricles voxels. The functional connectivity between homologous regions was calculated by the RV coefficient after different filtering stages.

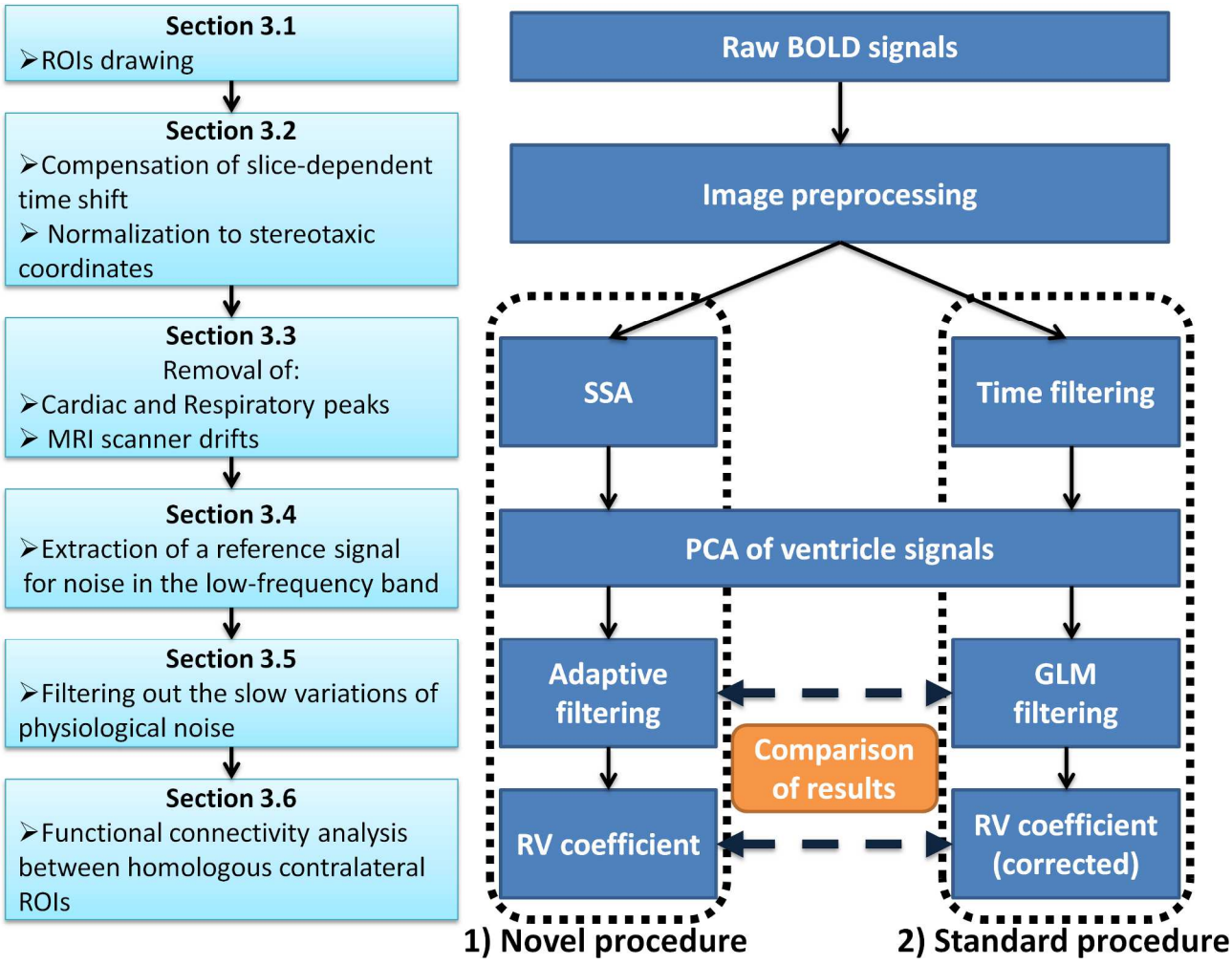

Figure 2. Flow diagram of different procedures for processing the BOLD signal in resting state conditions.

After the same preprocessing stage, two distinct main lines were followed for processing BOLD signal with different techniques. Results after the filtering stage (adaptive filtering and GLM filtering) and functional connectivity estimates (using the ordinary and the corrected RV coefficient) were balanced between the novel procedure (SSA & adaptive filtering) and the standard procedure (band-pass filtering & GLM) in order to highlight the method that removed the greatest amount of noise in the LFB and gave the highest contrast between WM and GM regions, according to the functional connectivity between homologous contralateral ROIs. The numbers within each box on the left side refer to the related subsections in the main text.

3.1 Resting state data and ROIs definition

Eight resting state fMRI recordings were acquired from healthy subjects (3 F, mean age ± SD = 24 ± 3 years) in order to validate the proposed procedure of BOLD signal analysis (SSA & adaptive filtering) with respect to the standard processing. For the method validation, high-frequency data acquisitions were performed in order to avoid aliasing effects of cardiac (~1 Hz) and respiratory (0.15-0.40 Hz) components in the LFB (<0.1 Hz) [52]: therefore, fMRI data have been acquired with a sampling rate of TR = 300 ms instead of typical longer TRs of standard scans (approximately 2000 ms). However, the choice of such low TR limited the acquisition to four slices instead of the whole brain coverage. A 1.5 Tesla GE scanner (General Electric, Milwaukee, WI) was used to acquire data for about ten min (1970 time points) with a GR-EPI sequence (FOV = 24 cm, TR/TE= 300/40 ms, FA = 90°, resolution = 64×64 pixels, voxel size 3.75×3.75×5 mm, REPS = 2000).

The four slices have been aligned to the anterior/posterior commissural line and selected so as to include Regions of Interest (ROIs) of grey matter involved in resting state functional networks according to the current literature [53]. Those included: Middle Prefrontal Cortex - MPFC - and insula (default mode network), Dorsolateral Prefrontal Cortex - DLPFC - (dorsal attentional network), Superior Temporal Sulcus - STS - and cuneus (ventral attentional network). Slices also included ROIs of white matter (anterior part of the semioval center) and lateral brain ventricles. In addition, for each subject a set of high resolution T1 weighted spoiled gradient recall images (1.2 mm thick axial slices; TR = 12.1 ms, TE = 5.22 ms, FA = 20°, FOV = 24 cm, resolution = 256×256 pixels) were acquired.

3.2 Image preprocessing

Functional data were preprocessed using the Analysis of Functional Neuroimaging (AFNI) software package [54]. Two main preprocessing steps have been performed: 1) compensation of slice-dependent time shift for aligning separate slices to the same temporal origin; 2) data normalization to the stereotaxic coordinates of Talairach and Tournoux atlas [55] with resampling to 1-mm cubic voxels. Neither spatial smoothing nor motion correction tasks were performed because, for the latter, the maximum displacement of subject head during scan sessions was below 0.7 mm.

3.3 Removal of physiological and instrumental noises

Herein, the SSA technique (paragraph 3.3.1) was used and compared to the *gold standard* band-pass filtering (paragraph 3.3.2). Both methodologies had the aim of removing noise components whose frequencies were outside the LFB, both at ultra-low (scanner drift related components) and high (respiratory and cardiac peaks) frequencies. Limits of the LFB were set at 0.04 and 0.10 Hz, respectively: the lower limit was set according to the recording length while the upper limit was chosen according to evidence from the literature of the neurovascular coupling dynamics, both during resting and activation states [3, 7].

3.3.1 Singular Spectrum Analysis

The SSA technique was employed to identify significant RCs in the LFB against the red noise null hypothesis. For the trajectory matrix size, the window length W was equal to 492 time points, nearly corresponding to ¼ of the time points in each recording. This length was chosen as a trade off between statistical confidence (number of columns of the trajectory matrix **D**) and frequency

resolution (related to the number of time points in each column of **D**, see paragraph 2.1.1). Furthermore, the window length W – which is also related to the lower bound for the LFB - was chosen as to include periodic oscillations with at least 5 periods within the time window. Since the frequency resolution was $(W \times TR)^{-1} \approx 0.007$ Hz, the lower limit of LFB was considered as $5*(W \times TR)^{-1} \approx 0.04$ Hz.

The identification of slow-varying RCs in the LFB was based on their dominant frequency. Using a forth-order AR model, the dominant frequency of each significant RC was taken as the frequency of the pair of poles, explaining more than 95% of the AR model variance. Only RCs with dominant frequency in the band 0.04 – 0.10 Hz were selected and voxels containing at least one slow-varying RC were considered as *active* in the LFB. For each *active* voxel, the significant RCs were summed in order to obtain the band-pass filtered signal in the LFB (i.e. LFB signal), according to SSA algorithm.

3.3.2 Band-pass time filtering

BOLD signals were detrended and filtered with standard algorithms for removing cardiac and respiratory components at their dominant frequencies, along with ultra-low frequency drifts due to hardware instability. The detrending task consisted in fitting and subtracting polynomials up to eight-order while a band-pass Butterworth filter with cutoff frequencies of 0.04-0.10 Hz was employed to remove the high frequency components. The lower limit was set to 0.04 Hz, thus equal to that of SSA processing. The filter order was set to 10 and a zero-phase digital filtering was obtained by processing the time course in both forward and reverse directions.

3.4 Extraction of a reference signal for noise in the LFB

Both SSA decomposition and band-pass filtering (steps 3.3.1 and 3.3.2, respectively) removed the cardiac and the respiratory components at their fundamental frequencies. However, other non-neuronal contributions such as those related to the heart beat variability [26] and to breath-to-breath variations [27], could still have been present in the LFB of BOLD signals. Therefore the brain ventricle signals were used in order to identify a reference signal related to these nuisance components, standing on the fact that only non-neuronal activities are expected in these regions. To this aim, PCA [37] was applied to the filtered time courses of ventricle voxels (both by SSA and by band-pass filtering) and the first PC was taken as the reference signal (REF) for the non-neuronal noise in the LFB.

The REF signal was then analyzed for non-stationary properties using a statistical test based on stationary time-frequency surrogates [56, 57]. This stationarity test compared the variability of the local amplitude of REF signal (i.e. the standard deviation of signal envelope) with those of its surrogates [58]. Namely, for each REF signal, the standard deviation (SD) of signal envelope (derived by Hilbert transform) was calculated and compared to the distribution of 10000 surrogates. Each surrogate was obtained from the REF signal by phase randomization in the Fourier domain. Since time-frequency surrogates were proved to be stationary signals [59], the 95^{th} percentile of their SD distribution was used as a threshold to test for REF stationarity, i.e., if the SD of REF signal was greater than the 95^{th} percentile of surrogates' distribution, the REF signal was considered a non-stationary signal.

3.5 Removal of noise in the LFB

Two different methodologies were employed and compared for removing the physiological noise in the LFB using REF signal: the standard GLM technique (3.5.1) and the novel approach based on adaptive filtering (3.5.2).

3.5.1 Nuisance Variable Regression

The former method was based on the NVR analysis [29] in which a GLM was estimated using the band-pass filtered signal as the dependent variable and the REF signal as the covariate in the model. The residual signal was then taken as the filtered signal in which the physiological noise was suppressed in the LFB by the GLM technique.

3.5.2 Adaptive filtering

The adaptive filter used REF signal as the reference signal for filtering the time courses of *active* voxels by SSA. The adaptive filter consisted of a 20-order FIR filter with a transversal structure and the nLMS adaptation algorithm (step size = 1) was employed for updating filter weights.

3.6 Estimation of the functional connectivity

For each subject, the functional connectivity [8] among brain regions was assessed using the processed BOLD signals belonging to grey matter (GM) and white matter (WM) regions, at the end of both novel and standard procedures. In particular, the functional connectivity was estimated between homologous contralateral ROIs since resting state networks were proved to have

symmetrical properties (e.g. left and right somatomotor [3], visual, auditory and sensorimotor cortices [7]). Pairs of ROI belonging to GM and WM regions were selected since higher values of correlation are expected between GM homologous regions due to the neuronal activity, whereas lower values are expected between WM regions where no functional connectivity should be present. Consequently, a higher connectivity in GM regions compared to WM regions has been considered as the outcome feature for comparing different procedures. Therefore, the contrast between GM and WM connectivity estimates was used in order to identify the procedure that provides the neatest functional connectivity maps.

Two indices were employed for quantifying the connectivity strength between the contralateral ROIs: the standard seed voxel correlation and the RV coefficient. The former consisted in averaging the filtered signals in the left and right hemispheres and estimating the temporal correlation between the resulting mean signals. The correlation coefficient was then squared (R^2) in order to quantify the proportion of shared variance between the time courses of homologous ROIs in different hemispheres. The RV coefficient was calculated with and without correction for the number of signals in the contralateral ROIs: indeed, SSA restricted the analysis only to *active* voxels whereas the standard procedure used all available voxels.

3.7 Statistical Analysis

Performances of the processing methods were assessed both on the evaluation of noise filtering and of the quality of the functional connectivity. For the former, variance changes of the filtered signals (for the statistical testing, the variance values have been logarithmic transformed in order to correct the skewness of the distribution) were considered, whereas the corrected RV coefficients (calculated between contralateral ROIs) were compared between the procedures. In addition, in order to describe the application of SSA on BOLD data, the descriptive statistics of the estimated parameters (autocorrelation and variance of noise, number of significant components and variance of filtered signal by SSA) were also reported.

The comparison of each feature as a function of ROI typology and processing method was performed by means of the analysis of variance (ANOVA) design, using subjects as a random factor in the model. Repeated measures ANOVA was employed to assess differences between processing methods among ROIs. For all features, preliminary tests were conducted using the Kolmogorov-Smirnov and the Levene's tests to check for data normality and homogeneity of variances, respectively. *Post-hoc* comparisons using the Bonferroni's correction of significance were conducted for significant ANOVA results: after correction, only *p*-values smaller than 0.05 were considered statistically significant.

Eta squared (η^2) index was employed to quantify the effect size in the ANOVA model for the functional connectivity estimates in the study group of eight subjects, in particular for measuring the contrast between WM and GM regions. Eta squared was calculated as the proportion of variance in the connectivity estimates that was explained by the type of ROI (i.e. WM and GM regions). Data are presented as mean ± SEM (Standard Error of the Mean) or mean ± SD (Standard Deviation), as indicated.

4. RESULTS AND DISCUSSION

4.1 SSA results

SSA was applied to BOLD signals in order to identify significant components (RCs) in the LFB compared to a null-hypothesis of autocorrelated noise. Figure 3 shows the results of SSA decomposition on a representative BOLD signal of a cuneus voxel.

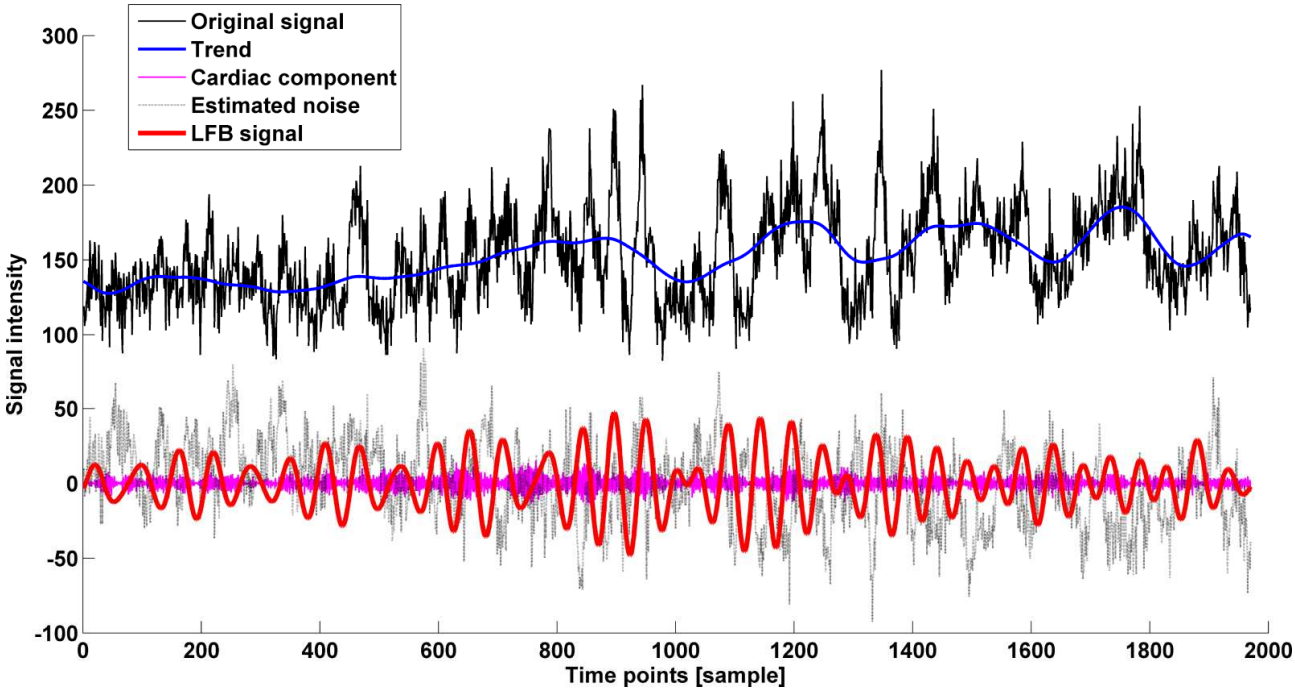

Figure 3. SSA decomposition of the time course of a cuneus active voxel (subject #1).

Original BOLD signal (black) is shown along with the extracted trend (blue), LFB signal (red), cardiac component (violet) and residual noise (black dotted line) obtained by SSA decomposition.

Extracted trend, LFB signal and cardiac components were obtained by summing the related significant RCs and identified according to their dominant frequency (see also Figure 1).

On average in the eight fMRI recordings, SSA algorithm identified 23.6% (range: 13.7-31.3%) of voxels as *active*, namely with at least one significant RC having the dominant frequency in the range 0.04−0.10 Hz. Among all ROIs, brain ventricles showed a significant greater proportion of *active* voxels than other regions (adj. $p<0.01$), while DLPFC and WM showed a slight lower ratio as compared to other GM regions (Table 1).

Table 1. Number of active voxels in the LFB (0.04−0.10 Hz) as detected by SSA algorithm applied to the BOLD signals of each subject. Data are expressed also as percentage of the number of voxels in the specific ROI and as a mean ± standard deviation (SD) over the entire study group.

	WM	Cuneus	DLPFC	Insula	MPFC	STS	Brain ventricles
Subject #1	26 (23.6%)	42 (27%)	28 (12.5%)	35 (17.5%)	12 (9.8%)	33 (14.5%)	28 (32.1%)
Subject #2	4 (4.7%)	48 (29.6%)	10 (3.5%)	27 (23.2%)	9 (7.2%)	33 (18.3%)	54 (71.0%)
Subject #3	13 (13.9%)	5 (2.6%)	21 (8.9%)	17 (10.3%)	37 (18.8%)	23 (9.5%)	45 (42.0%)
Subject #4	16 (12.5%)	59 (50.4%)	116 (22.8%)	47 (31.1%)	19 (19.0%)	39 (24.6%)	13 (17.5%)
Subject #5	11 (11.2%)	41 (18.5%)	104 (30.2%)	49 (33.1%)	28 (21.8%)	57 (27.1%)	66 (49.6%)
Subject #6	15 (26.7%)	115 (35.9%)	98 (18.3%)	46 (28.7%)	53 (26.3%)	81 (39.9%)	93 (76.2%)
Subject #7	21 (18.2%)	89 (33.5%)	26 (7.7%)	46 (18.1%)	27 (12.7%)	53 (19.5%)	19 (26.0%)
Subject #8	17 (26.1%)	83 (32.8%)	97 (17.7%)	130 (42.0%)	37 (35.2%)	79 (43.8%)	45 (72.5%)
Mean ± SD	17.1 ± 7.9%	28.8 ± 13.8%	15.2 ± 8.7%	25.5 ± 10.1%	18.8 ± 9.1%	24.6 ± 11.9%	48.4 ± 22.7%

The lag-1 autocorrelation parameter (γ) and the variance (α) of the noise model estimated by SSA algorithm showed also significant differences among ROIs. For the former parameter, WM, insula and STS regions showed significant lower values than other ROIs (adj. $p<0.01$) whereas the cuneus regions exhibited the highest mean value (mean ± SEM, 0.21 ± 0.02). However, the lag-1 autocorrelation parameter γ - that corresponds to the characteristic time decay τ of the red noise autocorrelation function - gave an estimate equal to $\tau = -1/log(\gamma) = -1/log(0.21) \approx 0.64$ samples for the cuneus regions, thus indicating a time decay smaller than one time sample. Therefore it can be stated that noise autocorrelation properties did not differ among ROIs, even though estimated values resulted significantly different. On the other hand, the noise variance α of brain ventricle regions was significantly greater than all GM regions (23.89 ± 1.53, adj. $p<0.01$) while the WM regions showed on average the lowest value (10.79 ± 0.11, adj. $p<0.01$).

Figure 4 shows the signal variance of LFB signal (i.e. the sum of all significant RCs obtained by SSA decomposition in the LFB), as well as the corresponding number of significant RCs identified in each *active* voxel.

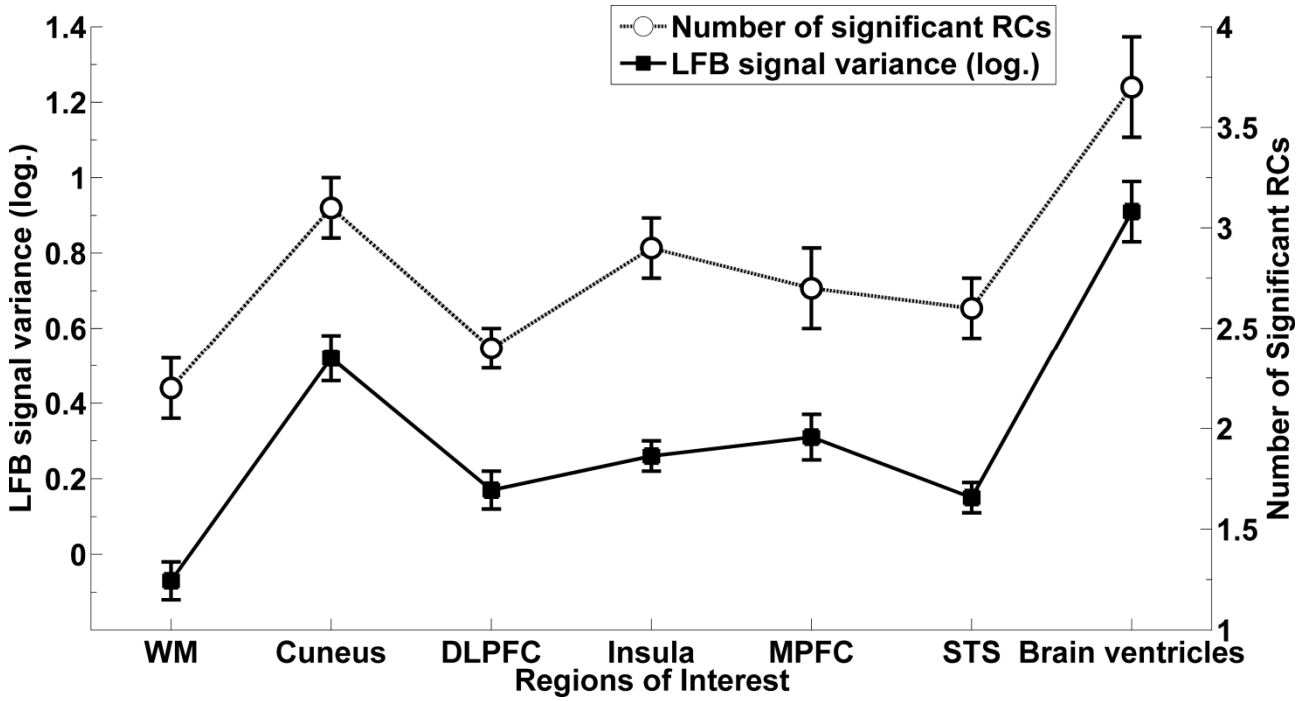

Figure 4. Signal features of the time course of active voxels identified by SSA.

The signal variance (black sqares, log_{10} values, left y-axis) and the number of significant RCs (white circles, right y-axis) of the time course of active voxels are plotted for each preselected ROI (x-axis) in the entire study group. Data are expressed as mean with 95% confidence interval.

Similarly to what obtained for the noise variance α, brain ventricle regions showed the greatest signal power and number of significant RCs in the LFB (signal variance: 0.91 ± 0.07, number of significant RCs: 3.7 ± 0.12 adj. $p<0.01$). Moreover, all GM regions exhibited greater values of signal power and number of RCs than WM regions (−0.07 ± 0.05 and 2.2 ± 0.09, adj. $p<0.05$). These findings corroborate the hypothesis that changes in blood volume at the capillary level and in the cerebrospinal fluid due to cardiovascular processes cause widespread global fluctuations related to the cardiac cycle, which tend to be spatially localized near ventricles, sulci, and large vessels. Indeed, the pulsatility of blood vessels induces an influx of desatured blood into the slice of interest, resulting in BOLD signal variations that tend to hide those related to neuronal

activities in GM regions [60, 61]. As a result, cardiac related displacements of cerebrospinal fluid are likely to generate significant spurious changes in BOLD signals. In a recent study [45], large negative correlations were also observed at 7 T in focal regions near ventricles, confirming the non-neuronal nature of these signal fluctuations due to hemodynamic changes and blood volume increase.

All these results (the highest proportion of *active* voxels, the largest noise variance and signal power in the LFB) indicate brain ventricles as regions corrupted by random and physiological noise, thus suitable for extracting a template of noise in the LFB.

4.2 Extraction of the noise template in the LFB

For each subject, Principal Component Analysis (PCA) was applied to the time courses of brain ventricle voxels in order to extract a template for the physiological noise in the LFB. This analysis was carried out both in the case of the band-pass filtering, using all available voxels) and in the case of SSA where only the extracted signals belonging to *active* voxels underwent the PCA. In the former case, the first PC (i.e. the *REF signal*) explained a mean (± SD) 46.0 ± 18.7% of the variance of brain ventricle signals while in the latter the percentage of explained variance was 48.6 ± 11.7%, that statistically did not differ from the standard procedure result ($p>0.05$).

The *scree* plot of PCs as well as the ventricle time courses and the first PC of Subject #5 are shown in Figure 5.

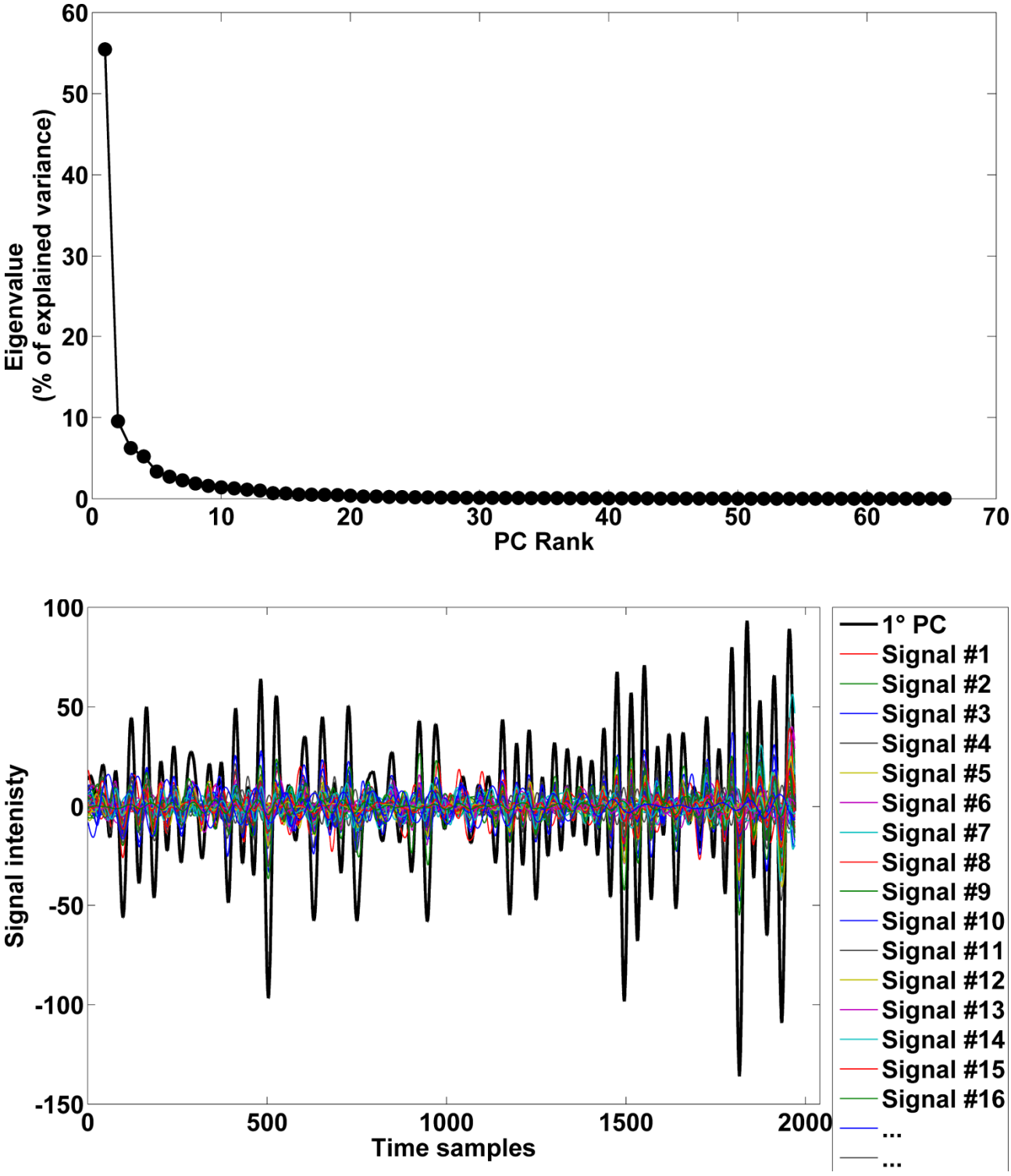

Figure 5. Results from PCA of brain ventricle signals (Subject #5).

<u>Upper panel</u>. Scree plot of PCA eigenvalues.

<u>Lower panel</u>. First 16 ventricle signals (out of 66) and the 1st PC (REF signal, black thick line).

In all subjects, the variability of the local amplitude of REF signal was greater than the 97.5th percentile of the distribution of its surrogates, proving that REF signal was a non-stationary signal (Table 2). For SSA processing, only in one case (subject #4) the REF signal was not significantly non-stationary: this may have been due to the small number of *active* voxels identified in the brain ventricle ROI of this subject (i.e., 13 voxels). The REF signal and its envelope, along with the distribution of surrogates' SD are shown in Figure 6.

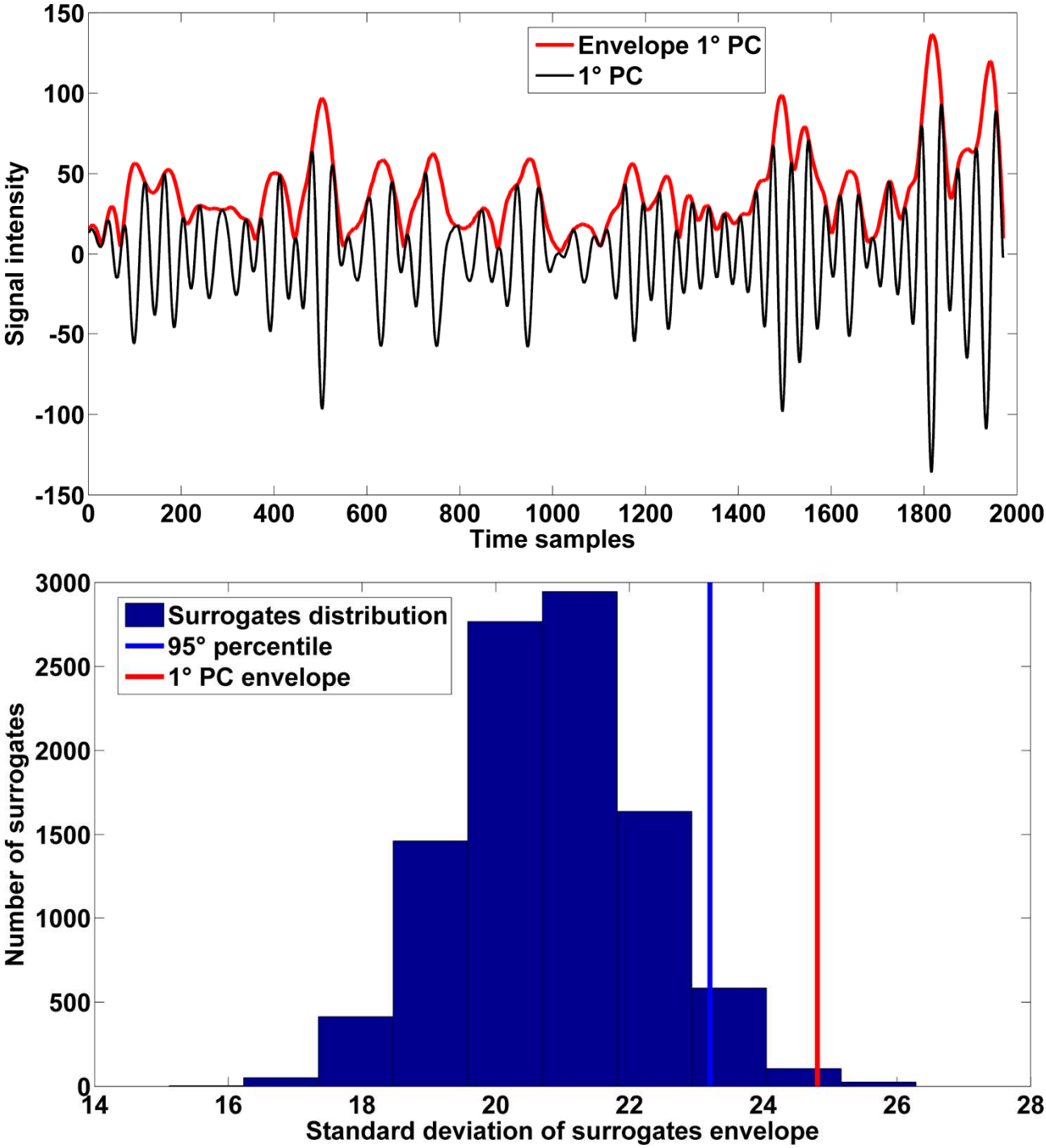

Figure 6. Results from the non-stationarity test of REF signal (Subject #5).

<u>Upper panel</u>. REF signal (black line) and its envelope obtained by Hilbert transform (red line).

<u>Lower panel</u>. Distribution of the standard deviation of surrogates' envelope. The 95th percentile of surrogates distribution (blue vertical line) and the SD value of REF signal (red line) are also shown.

These results suggest that REF signal may represent a suitable template for noise in the LFB, accounting for almost half the signals variability in brain ventricles voxels. Besides, the non-stationary nature of REF signal is compatible with the non-neuronal slow variations of physiological processes such as the heart rate variability, as well as the breath-to-breath respiratory changes. In fact, respiratory and cardiac processes are strictly related and both affect the blood flow and the CO_2 levels in the brain, which in turn determine relevant BOLD signal changes. Moreover, subject breathing may be associated to bulk motion of the head along with modulation of the magnetic field as a result of abdominal and thoracic movements, which can also lead to a shifting of the brain image [62, 63]. This may explain the presence of greater signal variance in ventricle regions that are located close to the edge of brain [27].

Table 2. Results of PCA applied to the time courses of brain ventricles, processed by SSA and by band-pass filtering (BPF). Results of the nonstationarity test based on time-frequency surrogates are also reported for the first PC (i.e. the REF signal). For SSA processing, the number of voxels used in the calculation refers only to active voxels in brain ventricle regions. (PC: Principal Component; SD: Standard Deviation)

Subject	Processing method	N° of brain ventricle voxels	Explained Variance by 1st PC (%)	SD of 1st PC envelope	97.5th percentile of surrogates SD distribution
#1	BPF	87	31.0	11.72*	9.96
	SSA	28	50.5	5.49*	4.75
#2	BPF	76	60.0	64.39*	45.06
	SSA	54	55.8	21.97*	15.67
#3	BPF	107	39.8	22.94*	18.66
	SSA	45	52.0	12.02*	10.56
#4	BPF	74	23.9	15.83*	12.05
	SSA	13	40.4	2.12	2.47
#5	BPF	133	76.2	72.76*	55.11
	SSA	66	55.7	24.81*	23.19
#6	BPF	122	39.1	53.46*	44.99
	SSA	93	42.2	20.14*	18.75
#7	BPF	73	65.3	31.63*	29.29
	SSA	19	65.4	13.43*	12.90
#8	BPF	62	32.8	28.29*	17.23
	SSA	45	27.2	11.47*	7.99

**: SD of the envelope of 1st PC greater than that obtained from surrogates distribution ($p<0.05$)*

4.3 Removal of physiological noise in the LFB

The REF signal was employed in two ways: as the covariate for NVR analysis (standard procedure) and as the reference signal of adaptive filter (novel procedure). In both cases, the efficacy of filtering noise in the LFB was quantified by computing the reduction of signal variance (ΔVAR%) before and after the filtering stage. The variance reduction was then normalized to the pre-filtering value and expressed as percentage. Figure 7 shows the reduction of signal variance (ΔVAR%) after both methodologies of processing and by using the REF signal as a template for noise in the LFB.

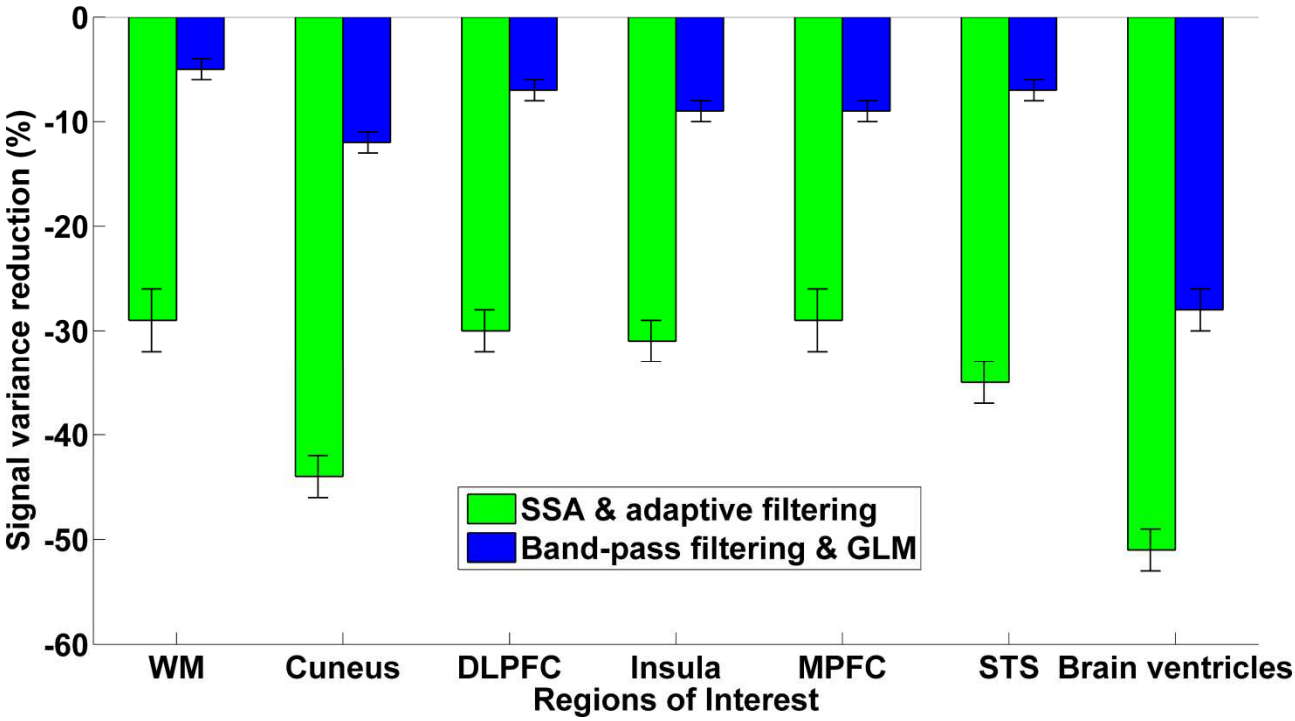

Figure 7. Performance of noise filtering by different procedures.

Reductions of signal variance (expressed as percent of pre-filtering variance, y-axis) after SSA & adaptive filtering (green, only active voxels) and after standard time filtering & GLM (blue, all available voxels) in the time courses belonging to eight ROIs (x-axis), by using the REF signal as a template for noise in the LFB. Data are expressed as mean with 95% confidence interval.

As expected, with both methods brain ventricle regions exhibited the most significant reductions of signal variance (adj. $p<0.01$) since the REF signal was used for filtering the time courses from which it had been derived. Also, the amount of variance reduction was highly correlated to the explained variance of REF signal in the brain ventricle region (correlation coefficients for all processing methods ranging from 0.64 to 0.75, $p<0.01$). Thus, the greater was the signal variability in the brain ventricles where only non-neuronal activity was present, the greater was the amount of noise in the time courses of other voxels in the brain that has been suppressed with filtering. The usage of SSA with adaptive filtering resulted in a significant greater variance reduction in every ROIs compared to the standard procedure based on the GLM of NVR analysis (overall, −43.9% vs. −10.1% respectively, $p<0.01$). This result suggests that adaptive filtering better removed the physiological noise from the time courses of other voxels, taking into account the time-frequency properties of REF signal. Indeed, it has been proved that adaptive methods exhibits good performance in suppressing cardiac and respiratory artifacts in the image domain [64] and to be specifically suited on identifying cardiac arrhythmias during real-time fMRI [65]. Furthermore, the greater reduction of noise performed by adaptive filtering could be even more useful in experiments with higher field strength (3 T or 7 T) since the physiological noise contribution was proved to increases accordingly [66]. Unlike NVR, these results demonstrate the high capability of adaptive filtering in following the non-stationary characteristics of physiological processes, thus make it suitable for properly removing the cardio-respiratory noise in the LFB of BOLD signal.

4.4 Functional connectivity

The functional connectivity of homologous contralateral ROIs was quantified by the seed-voxel correlation and by the RV coefficient. The functional connectivity estimates were calculated in two conditions: after SSA & adaptive filtering and after the standard time filtering & GLM (Figure 8).

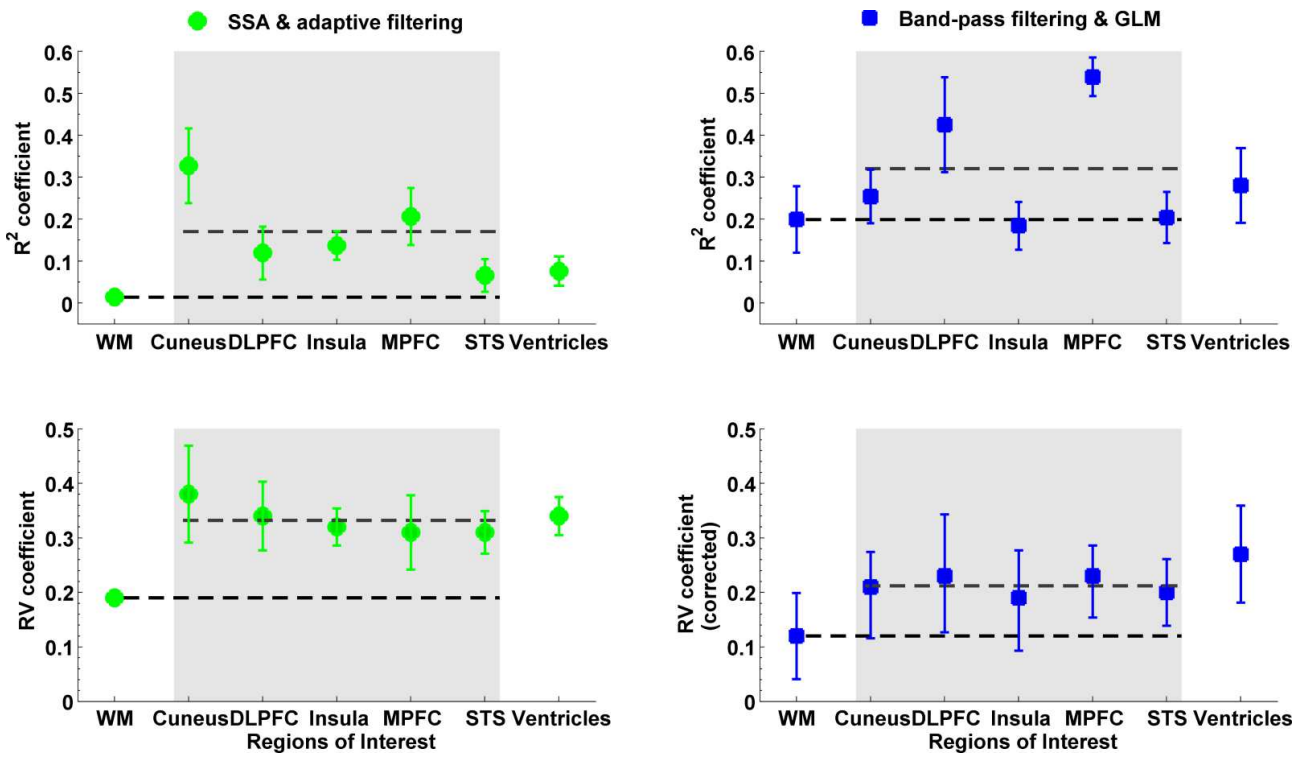

Figure 8. Functional connectivity estimates between homologous contralateral ROIs.

In each graph, the grey area identify GM regions, lower black dotted lines represent the mean connectivity of WM regions; upper grey dotted lines identify the average connectivity in GM regions. Data are presented as mean values ± SEM in the group of eight subjects.

<u>Upper panels</u>. R^2 coefficients (y-axis) between mean signals of homologous ROIs (x-axis) after SSA & adaptive filtering (using only active voxels, green circles, left panel) and after band-pass time filtering & GLM (considering all available voxels, blue squares, right panel).

<u>Lower panels</u>. RV coefficients (y-axis) between homologous ROIs (x-axis) after SSA & adaptive filtering (using only active voxels, green circles, left panel) and corrected RV coefficients (y-axis) between homologous ROIs (x-axis) after band-pass filtering & GLM (same number of active voxels as in the SSA case, blue squares, right panel).

As a result of the seed voxel method (Figure 8, upper panels), the novel procedure based on *active* voxels showed a better separation between GM and WM than the standard processing (η^2 = 32% vs. η^2 = 26%, respectively). However, the seed voxel correlation gives an overall estimate of the connectivity due to signals averaging, thus it did not consider the different number of time courses of the two procedures, as well as the specific voxels which contributed to the resulting R^2 values. Therefore, the RV coefficient was also employed as an index of functional connectivity, taking into account each single time course belonging to the contralateral ROIs.

On average, SSA & adaptive filtering showed significant lower RV coefficients than the standard time filtering & GLM (adj. p<0.01, results not shown). However, lower RV coefficients in the case of SSA could have been related to the smaller number of voxels used in the computation (i.e. only the *active* voxels), hence the proposed Monte Carlo resampling method was applied to the signals processed with the standard procedure, using the same number of *active* voxels identified by SSA. The *corrected* RV coefficients were computed for each subject and type of ROI and compared to those obtained by SSA processing. As a result, the mean *corrected* RV coefficients of standard processing were significantly lower than the corresponding RV coefficients by SSA, considering the same number of *active* voxels (adj. p<0.05 for all ROI pairs). Furthermore, RV coefficients in the case of the novel procedure provided a higher contrast among ROIs (η^2 = 35%) than the standard procedure using the *corrected* RV coefficient (η^2 = 28%) (Figure 8, lower panels). In particular, the mean RV coefficient of WM regions in the case of SSA processing was significantly lower than those related to the GM regions (adj. p<0.01), thus corroborating the hypothesis of small (or even absent) coupling in WM regions where no neuronal activity is expected. These results also indicate that SSA identified only the voxels in the GM regions that contributed to the neural coupling between homologous ROIs, resulting in higher RV coefficients than those obtained using the standard procedure on all available voxels. It might be speculated that in case of longer TRs and a greater number of acquired voxels, the application of SSA could also give better results in terms

of thresholding the functional connectivity maps. Indeed, by restricting the statistical analyses only to a small fraction of acquired voxels (*active* voxels), the threshold value for the test statistic could lead to a smaller number of false positives, using the same significance level. Therefore SSA could be a useful method for improving the determination of thresholds for a statistical map, along with the false discovery rate [67] or the random field approach [24].

Nevertheless, the relative high values of RV coefficients of brain ventricles indicated a residual coupling between these non-neuronal regions, probably due to the incomplete removal of the physiological noise. This hypothesis is supported by the fact that REF signal explained only half the variability of brain ventricles signals (on average, 48.6%), thus not all the noise was removed by the adaptive filtering. One possible approach to overcome this issue could be performing sequential stages of adaptive filtering using the first two or three PCs of brain ventricle time courses, in order to achieve a better suppression of the physiological noise in the LFB.

5. CONCLUSIONS

The application of SSA to the BOLD signal in resting state condition led to the identification of *active* voxels in the LFB (<0.1 Hz) by extracting slow-varying components, which showed significant higher signal power against a null hypothesis of autocorrelated noise. The adaptive filtering took into account the non-stationary characteristics of physiological noise in the LFB, allowing a better filtering of the signals belonging to GM and WM regions. Furthermore, a corrected version for the RV coefficient was employed in order to assess the functional connectivity between homologous regions and to balance results of the standard procedure (which considered all available voxels) with those of the novel procedure, based only on *active* voxels.

As a result, SSA & adaptive filtering achieved a greater reduction of noise in all regions (−43.9% vs. −10.1%) and led to a higher contrast between GM and WM functional connectivity (35% vs. 28%) than the standard procedure (band-pass time filtering & GLM). These results suggest that the combination of SSA and adaptive filtering is a reasonable and convenient approach for removing the low-frequency fluctuations of BOLD signal due to physiological noise, and to emphasize the functional networks in resting state. Further studies should be carried out to explore the feasibility of the proposed method on datasets with higher TRs, with a higher number of subjects and on higher magnetic fields.

6. REFERENCES

[1] P. A. Bandettini, A. Jesmanowicz, E. C. Wong, and J. S. Hyde, "Processing strategies for time-course data sets in functional MRI of the human brain," *Magn Reson Med,* vol. 30, pp. 161-73, Aug 1993.

[2] G. M. Boynton, S. A. Engel, G. H. Glover, and D. J. Heeger, "Linear systems analysis of functional magnetic resonance imaging in human V1," *J Neurosci,* vol. 16, pp. 4207-21, Jul 1 1996.

[3] B. Biswal, F. Z. Yetkin, V. M. Haughton, and J. S. Hyde, "Functional connectivity in the motor cortex of resting human brain using echo-planar MRI," *Magn Reson Med,* vol. 34, pp. 537-41, Oct 1995.

[4] M. J. Lowe, B. J. Mock, and J. A. Sorenson, "Functional connectivity in single and multislice echoplanar imaging using resting-state fluctuations," *Neuroimage,* vol. 7, pp. 119-32, Feb 1998.

[5] J. Xiong, L. M. Parsons, J. H. Gao, and P. T. Fox, "Interregional connectivity to primary motor cortex revealed using MRI resting state images," *Hum Brain Mapp,* vol. 8, pp. 151-6, 1999.

[6] T. T. Dang-Vu, M. Schabus, M. Desseilles, G. Albouy, M. Boly, A. Darsaud, S. Gais, G. Rauchs, V. Sterpenich, G. Vandewalle, J. Carrier, G. Moonen, E. Balteau, C. Degueldre, A. Luxen, C. Phillips, and P. Maquet, "Spontaneous neural activity during human slow wave sleep," *Proc Natl Acad Sci U S A,* vol. 105, pp. 15160-5, Sep 30 2008.

[7] D. Cordes, V. M. Haughton, K. Arfanakis, J. D. Carew, P. A. Turski, C. H. Moritz, M. A. Quigley, and M. E. Meyerand, "Frequencies contributing to functional connectivity in the cerebral cortex in "resting-state" data," *AJNR Am J Neuroradiol,* vol. 22, pp. 1326-33, Aug 2001.

[8] K. J. Friston, "Functional and effective connectivity in neuroimaging: A synthesis," *Human Brain Mapping*, vol. 2, pp. 56-78, 1994.

[9] D. Cordes, V. M. Haughton, K. Arfanakis, G. J. Wendt, P. A. Turski, C. H. Moritz, M. A. Quigley, and M. E. Meyerand, "Mapping functionally related regions of brain with functional connectivity MR imaging," *AJNR Am J Neuroradiol*, vol. 21, pp. 1636-44, Oct 2000.

[10] J. S. Damoiseaux, S. A. Rombouts, F. Barkhof, P. Scheltens, C. J. Stam, S. M. Smith, and C. F. Beckmann, "Consistent resting-state networks across healthy subjects," *Proc Natl Acad Sci U S A*, vol. 103, pp. 13848-53, Sep 12 2006.

[11] M. De Luca, C. F. Beckmann, N. De Stefano, P. M. Matthews, and S. M. Smith, "fMRI resting state networks define distinct modes of long-distance interactions in the human brain," *Neuroimage*, vol. 29, pp. 1359-67, Feb 15 2006.

[12] M. D. Fox, A. Z. Snyder, J. L. Vincent, M. Corbetta, D. C. Van Essen, and M. E. Raichle, "The human brain is intrinsically organized into dynamic, anticorrelated functional networks," *Proc Natl Acad Sci U S A*, vol. 102, pp. 9673-8, Jul 5 2005.

[13] M. E. Raichle, A. M. MacLeod, A. Z. Snyder, W. J. Powers, D. A. Gusnard, and G. L. Shulman, "A default mode of brain function," *Proc Natl Acad Sci U S A*, vol. 98, pp. 676-82, Jan 16 2001.

[14] P. Fransson, "Spontaneous low-frequency BOLD signal fluctuations: an fMRI investigation of the resting-state default mode of brain function hypothesis," *Hum Brain Mapp*, vol. 26, pp. 15-29, Sep 2005.

[15] P. Fransson, "How default is the default mode of brain function? Further evidence from intrinsic BOLD signal fluctuations," *Neuropsychologia*, vol. 44, pp. 2836-45, 2006.

[16] M. D. Greicius, B. Krasnow, A. L. Reiss, and V. Menon, "Functional connectivity in the resting brain: a network analysis of the default mode hypothesis," *Proc Natl Acad Sci U S A,* vol. 100, pp. 253-8, Jan 7 2003.

[17] K. J. Friston, J. T. Ashburner, S. J. Kiebel, T. E. Nichols, and W. D. Penny, *Statistical parametric mapping: the analysis of funtional brain images*: Elsevier/Academic Press, 2007.

[18] C. F. Beckmann, M. DeLuca, J. T. Devlin, and S. M. Smith, "Investigations into resting-state connectivity using independent component analysis," *Philos Trans R Soc Lond B Biol Sci,* vol. 360, pp. 1001-13, May 29 2005.

[19] C. F. Beckmann and S. M. Smith, "Probabilistic independent component analysis for functional magnetic resonance imaging," *IEEE Trans Med Imaging,* vol. 23, pp. 137-52, Feb 2004.

[20] R. M. Birn, K. Murphy, and P. A. Bandettini, "The effect of respiration variations on independent component analysis results of resting state functional connectivity," *Hum Brain Mapp,* vol. 29, pp. 740-50, Jul 2008.

[21] J. S. Damoiseaux, C. F. Beckmann, E. J. Arigita, F. Barkhof, P. Scheltens, C. J. Stam, S. M. Smith, and S. A. Rombouts, "Reduced resting-state brain activity in the "default network" in normal aging," *Cereb Cortex,* vol. 18, pp. 1856-64, Aug 2008.

[22] M. D. Fox, D. Zhang, A. Z. Snyder, and M. E. Raichle, "The global signal and observed anticorrelated resting state brain networks," *J Neurophysiol,* vol. 101, pp. 3270-83, Jun 2009.

[23] D. Mantini, M. G. Perrucci, C. Del Gratta, G. L. Romani, and M. Corbetta, "Electrophysiological signatures of resting state networks in the human brain," *Proc Natl Acad Sci U S A,* vol. 104, pp. 13170-5, Aug 7 2007.

[24] K. J. Worsley, S. Marrett, P. Neelin, A. C. Vandal, K. J. Friston, and A. C. Evans, "A unified statistical approach for determining significant signals in images of cerebral activation," *Hum Brain Mapp,* vol. 4, pp. 58-73, 1996.

[25] C. Chang, J. P. Cunningham, and G. H. Glover, "Influence of heart rate on the BOLD signal: the cardiac response function," *Neuroimage,* vol. 44, pp. 857-69, Feb 1 2009.

[26] K. Shmueli, P. van Gelderen, J. A. de Zwart, S. G. Horovitz, M. Fukunaga, J. M. Jansma, and J. H. Duyn, "Low-frequency fluctuations in the cardiac rate as a source of variance in the resting-state fMRI BOLD signal," *Neuroimage,* vol. 38, pp. 306-20, Nov 1 2007.

[27] R. M. Birn, J. B. Diamond, M. A. Smith, and P. A. Bandettini, "Separating respiratory-variation-related fluctuations from neuronal-activity-related fluctuations in fMRI," *Neuroimage,* vol. 31, pp. 1536-48, Jul 15 2006.

[28] R. G. Wise, K. Ide, M. J. Poulin, and I. Tracey, "Resting fluctuations in arterial carbon dioxide induce significant low frequency variations in BOLD signal," *Neuroimage,* vol. 21, pp. 1652-64, Apr 2004.

[29] T. E. Lund, K. H. Madsen, K. Sidaros, W. L. Luo, and T. E. Nichols, "Non-white noise in fMRI: does modelling have an impact?," *Neuroimage,* vol. 29, pp. 54-66, Jan 1 2006.

[30] K. J. Friston, A. P. Holmes, J. B. Poline, P. J. Grasby, S. C. Williams, R. S. Frackowiak, and R. Turner, "Analysis of fMRI time-series revisited," *Neuroimage,* vol. 2, pp. 45-53, Mar 1995.

[31] C. J. Long, E. N. Brown, C. Triantafyllou, I. Aharon, L. L. Wald, and V. Solo, "Nonstationary noise estimation in functional MRI," *Neuroimage,* vol. 28, pp. 890-903, Dec 2005.

[32] R. M. Birn, K. Murphy, D. A. Handwerker, and P. A. Bandettini, "fMRI in the presence of task-correlated breathing variations," *Neuroimage,* vol. 47, pp. 1092-104, Sep 2009.

[33] N. Golyandina, V. V. Nekrutkin, and A. A. Zhigliavski *Analysis of time series structure: SSA and related techniques* vol. 90: CRC Press, 2001.

[34] S. S. Haykin, *Adaptive filter theory*: Prentice Hall, 2002.

[35] J. B. Elsner and A. A. Tsonis, *Singular spectrum analysis: a new tool in time series analysis*: Plenum Publishing Corporation, 1996.

[36] M. Ghil, M. Allen, M. Dettinger, K. Ide, D. Kondrashov, M. Mann, A. Robertson, A. Saunders, Y. Tian, and F. Varadi, "Advanced spectral methods for climatic time series," *Rev. Geophys,* vol. 40, p. 1003, 2002.

[37] I. T. Jolliffe, *Principal component analysis*: Springer-Verlag, 2002.

[38] H. F. Kaiser, "The varimax criterion for analytic rotation in factor analysis," *Psychometrika,* vol. 23, pp. 187-200, 1958.

[39] R. Catell, "The scree test for the number of factors," *Multivariate behavioral research,* vol. 1, pp. 245-276, 1966.

[40] M. R. Allen and L. A. Smith, "Monte Carlo SSA: detecting irregular oscillations in the presence of coloured noise," *Journal of Climate,* vol. 9, pp. 3373-3404, 1996.

[41] C. Chatfield, *The analysis of time series: an introduction,* 6 ed. vol. 59: CRC press, 2004.

[42] J. P. Burg, "Maximum entropy spectral analysis," 1967.

[43] R. Vautard, P. Yiou, and M. Ghil, "Singular-spectrum analysis: A toolkit for short, noisy chaotic signals," *Physica D: Nonlinear Phenomena,* vol. 58, pp. 95-126, 1992.

[44] Q. Zhang, G. E. Strangman, and G. Ganis, "Adaptive filtering to reduce global interference in non-invasive NIRS measures of brain activation: how well and when does it work?," *Neuroimage,* vol. 45, pp. 788-94, Apr 15 2009.

[45] M. Bianciardi, M. Fukunaga, P. van Gelderen, J. A. de Zwart, and J. H. Duyn, "Negative BOLD-fMRI signals in large cerebral veins," *J Cereb Blood Flow Metab,* vol. 31, pp. 401-12, Feb 2011.

[46] M. S. Dagli, J. E. Ingeholm, and J. V. Haxby, "Localization of cardiac-induced signal change in fMRI," *Neuroimage,* vol. 9, pp. 407-15, Apr 1999.

[47] M. H. Hayes, *Statistical digital signal processing and modeling*: John Wiley & Sons, 1996.

[48] P. Robert and Y. Escoufier, "A unifying tool for linear multivariate statistical methods: the RV-coefficient," *Journal of the Royal Statistical Society. Series C (Applied Statistics),* vol. 25, pp. 257-265, 1976.

[49] H. Zhang, J. Tian, J. Li, and J. Zhao, "RV-coefficient and its significance test in mapping brain functional connectivity," 2009, p. 726222.

[50] F. Kherif, J. B. Poline, S. Meriaux, H. Benali, G. Flandin, and M. Brett, "Group analysis in functional neuroimaging: selecting subjects using similarity measures," *Neuroimage,* vol. 20, pp. 2197-208, Dec 2003.

[51] H. Abdi, J. P. Dunlop, and L. J. Williams, "How to compute reliability estimates and display confidence and tolerance intervals for pattern classifiers using the Bootstrap and 3-way multidimensional scaling (DISTATIS)," *Neuroimage,* vol. 45, pp. 89-95, Mar 1 2009.

[52] T. E. Lund, "fcMRI--mapping functional connectivity or correlating cardiac-induced noise?," *Magn Reson Med,* vol. 46, pp. 628-9, Sep 2001.

[53] M. D. Fox and M. E. Raichle, "Spontaneous fluctuations in brain activity observed with functional magnetic resonance imaging," *Nat Rev Neurosci,* vol. 8, pp. 700-11, Sep 2007.

[54] R. W. Cox, "AFNI: software for analysis and visualization of functional magnetic resonance neuroimages," *Comput Biomed Res,* vol. 29, pp. 162-73, Jun 1996.

[55] J. Talairach and P. Tournoux, *Co-planar stereotaxic atlas of the human brain: 3-dimensional proportional system : an approach to cerebral imaging*: G. Thieme, 1988.

[56] P. Borgnat, P. Flandrin, P. Honeine, C. Richard, and X. Jun, "Testing Stationarity With Surrogates: A Time-Frequency Approach," *Signal Processing, IEEE Transactions on,* vol. 58, pp. 3459-3470, 2010.

[57] T. Schreiber and A. Schmitz, "Surrogate time series," *Physica D: Nonlinear Phenomena*, vol. 142, pp. 346-382, 2000.

[58] P. Piaggi, D. Menicucci, C. Gentili, G. Handjaras, M. Laurino, A. Piarulli, M. Guazzelli, A. Gemignani, and A. Landi, "Adaptive Filtering for Removing Nonstationary Physiological Noise from Resting State fMRI BOLD Signals," in *11th International Conference on Intelligent Systems Design and Applications (ISDA), 2011*, Córdoba, Spain, 2011, pp. 237-241.

[59] C. Richard, A. Ferrari, H. Amoud, P. Honeine, P. Flandrin, and P. Borgnat, "Statistical hypothesis testing with time-frequency surrogates to check signal stationarity," in *Acoustics Speech and Signal Processing (ICASSP), 2010 IEEE International Conference on*, 2010, pp. 3666-3669.

[60] J. E. A. O'Connell, "The vascular factor in intracranial pressure and the maintenance of the cerebrospinal fluid circulation," *Brain,* vol. 66, pp. 204-228, September 1, 1943 1943.

[61] M. Piche, J. Cohen-Adad, M. K. Nejad, V. Perlbarg, G. Xie, G. Beaudoin, H. Benali, and P. Rainville, "Characterization of cardiac-related noise in fMRI of the cervical spinal cord," *Magn Reson Imaging,* vol. 27, pp. 300-10, Apr 2009.

[62] D. Raj, A. W. Anderson, and J. C. Gore, "Respiratory effects in human functional magnetic resonance imaging due to bulk susceptibility changes," *Phys Med Biol,* vol. 46, pp. 3331-40, Dec 2001.

[63] C. Windischberger, H. Langenberger, T. Sycha, E. M. Tschernko, G. Fuchsjager-Mayerl, L. Schmetterer, and E. Moser, "On the origin of respiratory artifacts in BOLD-EPI of the human brain," *Magn Reson Imaging,* vol. 20, pp. 575-82, Oct 2002.

[64] R. H. Deckers, P. van Gelderen, M. Ries, O. Barret, J. H. Duyn, V. N. Ikonomidou, M. Fukunaga, G. H. Glover, and J. A. de Zwart, "An adaptive filter for suppression of cardiac and respiratory noise in MRI time series data," *Neuroimage,* vol. 33, pp. 1072-81, Dec 2006.

[65] V. Wu, I. M. Barbash, K. Ratnayaka, C. E. Saikus, M. Sonmez, O. Kocaturk, R. J. Lederman, and A. Z. Faranesh, "Adaptive noise cancellation to suppress electrocardiography artifacts during real-time interventional MRI," *J Magn Reson Imaging,* vol. 33, pp. 1184-93, May 2011.

[66] C. Triantafyllou, R. D. Hoge, G. Krueger, C. J. Wiggins, A. Potthast, G. C. Wiggins, and L. L. Wald, "Comparison of physiological noise at 1.5 T, 3 T and 7 T and optimization of fMRI acquisition parameters," *Neuroimage,* vol. 26, pp. 243-50, May 15 2005.

[67] C. R. Genovese, N. A. Lazar, and T. Nichols, "Thresholding of statistical maps in functional neuroimaging using the false discovery rate," *Neuroimage,* vol. 15, pp. 870-8, Apr 2002.

7. ACKNOWLEDGEMENTS

I wish to thank Dr. Danilo Menicucci for his useful comments and friendship and Prof. Alberto Landi for his guidance and constant availability: I could not have wished for better collaborator and tutor during these three years of PhD course!

Pisa, March 2012